nature communications

Article

https://doi.org/10.1038/s41467-024-55175-0

Future increase in compound soil drought-heat extremes exacerbated by vegetation greening

Received: 8 November 2024

Accepted: 4 December 2024

Jun Li[1], Yao Zhang[1] ✉, Emanuele Bevacqua[2], Jakob Zscheischler[2], Trevor F. Keenan[3,4], Xu Lian[5], Sha Zhou[6], Hongying Zhang[1], Mingzhu He[1,7] & Shilong Piao[1]

Compound soil drought and heat extremes are expected to occur more frequently with global warming, causing wide-ranging socio-ecological repercussions. Vegetation modulates air temperature and soil moisture through biophysical processes, thereby influencing the occurrence of such extremes. Global vegetation cover is broadly expected to increase under climate change, but it remains unclear whether vegetation greening will alleviate or aggravate future increases in compound soil drought-heat events. Here, using a suite of state-of-the-art model simulations, we show that the projected vegetation greening will increase the frequency of global compound soil drought-heat events, equivalent to 12–21% of the total increment at the end of 21st century. This increase is predominantly driven by reduced albedo and enhanced transpiration associated with increased leaf area. Although greening-induced transpiration enhancement has counteracting cooling and drying effects, the excessive water loss in the early growing season can lead to later soil moisture deficits, amplifying compound soil drought-heat extremes during the subsequent warm season. These changes are most pronounced in northern high latitudes and are dominated by the warming effect of CO_2. Our study highlights the necessity of integrating vegetation biophysical effects into mitigation and adaptation strategies for addressing compound climate risks.

Occurrences of compound soil drought-heat events, i.e., co-occurring low soil moisture and high-temperature extremes, have caused extensive crop failures, wildfires, ecosystem carbon losses, and even human mortality worldwide, posing a growing threat to human society and ecosystem resilience[1–4]. Compound soil drought-heat conditions are projected to increase in many regions during the 21st century, with important socio-ecological impacts[5–7]. Given the myriad of consequences, compound soil drought-heat events have gained significant attention from the scientific community, with particular focus on temporal and spatial variations[8,9], mechanisms related to land-atmosphere interactions[10,11], and the impacts on biophysical and biogeochemical processes[12]. However, a quantitative understanding of how long-term vegetation changes might impact the occurrence of compound soil drought-heat events is lacking.

---

[1]Institute of Carbon Neutrality, Sino-French Institute for Earth System Science, College of Urban and Environmental Sciences, Peking University, Beijing, China. [2]Department of Compound Environmental Risks, Helmholtz Centre for Environmental Research–UFZ, Leipzig, Germany. [3]Earth and Environmental Sciences Area, Lawrence Berkeley National Laboratory, Berkeley, CA, USA. [4]Department of Environmental Science Policy and Management, UC Berkeley, Berkeley, CA, USA. [5]Department of Earth and Environmental Engineering, Columbia University, New York, NY, USA. [6]State Key Laboratory of Earth Surface Processes and Resources Ecology, Faculty of Geographical Science, Beijing Normal University, Beijing, China. [7]School of National Safety and Emergency Management, Beijing Normal University, Zhuhai, China. ✉e-mail: zhangyao@pku.edu.cn

Changes in vegetation cover, productivity and water use have multiple impacts on climate, through modifying key surface biophysical properties such as transpiration and albedo[13] (Figs. 1a and Supplementary Fig. 1). These impacts can be categorized as both positive and negative climate feedbacks. For example, the projected increase in vegetation activity and extension of growing seasons can enhance transpiration, effectively dissipating extra heat and cooling the land surface[14–16]. In contrast, a denser vegetation canopy can absorb more heat into the land by reducing albedo, thereby warming the land surface[17]. Additionally, enhanced plant transpiration may accelerate soil drying and facilitate the occurrence of droughts[18,19]. Such effects may also propagate from previous seasons to later seasons through soil moisture memory effect[20,21]. As changes in compound soil drought-heat events are induced by variations in multiple drivers and their dependencies, the effects of vegetation on such events involve complex interactions among the aforementioned processes, which act either in synergy or counteractively. Moreover, while current attribution frameworks for univariate events provide useful insights, they cannot connect the multi-directional processes underlying vegetation effects or quantify compounding characteristics[22]. These complexities pose a major challenge in quantifying the risk of future compound soil drought-heat events associated with plant biophysics.

Here, we develop a framework to quantify the likelihood changes of compound soil drought-heat events from 1850-2100 and attribute these changes to transpiration (Tr) and albedo (α) effects, which are the two key land surface properties[23] through which vegetation regulates the land water and energy balance and thus air temperature (Ta) and soil moisture (SM)[14,24]. The compound soil drought-heat events are identified as co-occurring low SM and high Ta over the warm season (the climatologically hottest three consecutive months), which overlaps with the main growing season when plants are most active. By employing 17 state-of-the-art Earth system models (ESMs) from the Coupled Model Intercomparison Project Phase 6 (CMIP6) which incorporate current knowledge of various land processes[25], we characterize changes in the frequency of compound soil drought-heat extremes using the likelihood multiplication factor (LMF)[26]. LMF is defined as the ratio of the joint probability of low SM and high Ta between future and historical periods, which effectively characterizes the changes in the occurrence of compound extremes. We partition the LMF into two components: (1) those related to the trends of Ta and SM, and (2) those related to the variability and dependence of both variables (Figs. 1b–c and Supplementary Figs. 2a–b, Methods). We then attribute the LMF components to vegetation-induced changes in Tr and α. This allows us to comprehensively evaluate the effect of projected greening on the likelihood of compound extremes under future climate change, and identify the underlying processes driving these changes (see "Methods" for details).

Results

Increases in global compound soil drought-heat likelihood from vegetation biophysics

We estimate the changes in the likelihood of compound soil drought-heat events (represented by LMF) and their trend (t) and variability and dependency (vd) components throughout 1851-2100 relative to the 1850-1879 baseline (Fig. 2). For each component, we further delineate the contribution of vegetation change through its impact on α and Tr from both current (cur) and previous (pre) seasons. For the LMF induced by the trends of climate variables, the albedo effect ($\mathrm{LMF}^{t}_{cur-\alpha}$) exhibits a progressive increase during the 21st century, which dominates the overall increase in the likelihood of compound soil drought-

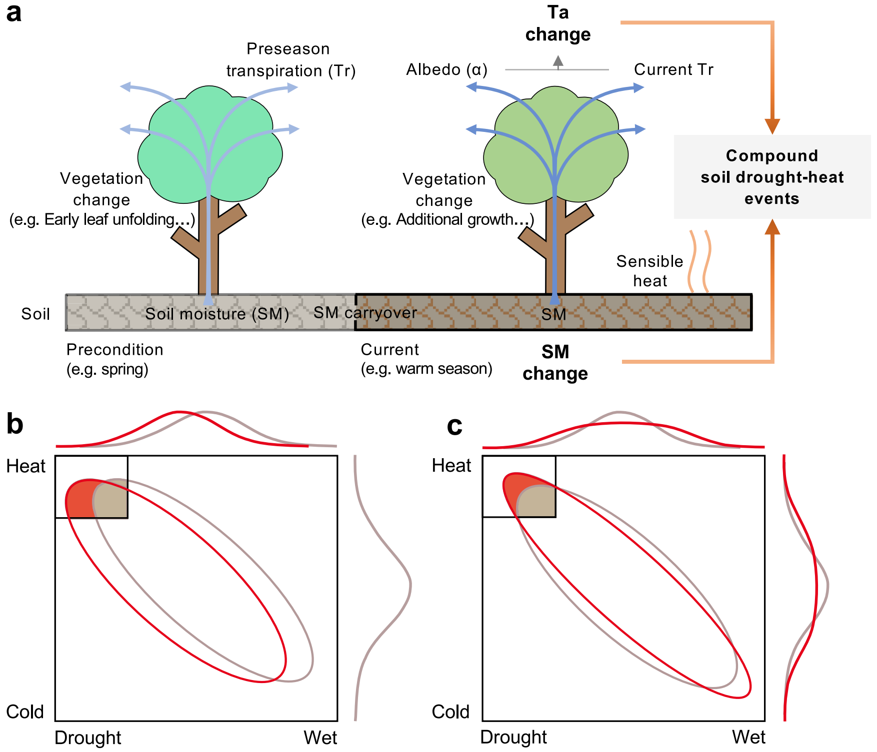

Fig. 1 | Schematic diagram for quantifying changes in the likelihood of compound soil drought-heat events attributed to vegetation biophysics. **a** Illustration of the effects of plant transpiration (Tr) and albedo (α) on compound soil drought-heat events through regulating temperature (Ta) and soil moisture (SM). For a comprehensive description of the processes involved, please refer to Supplementary Fig. 2a. **b**–**c** The hypothetical change in the likelihood of compound soil drought-heat events (shift of the bivariate distribution from gray to red) arising from a shift in the trend while holding the variability and dependence constant (**b**) and a shift in the variability and dependence while holding the trend constant (**c**). The black solid line in the upper left corner indicates a threshold assumed to be constant for both present and future climate conditions. Schematically, the likelihood of a compound soil drought-heat event (represented by LMF) represents the ratio of the area bounded by the red and black lines to the area enclosed by the gray and black lines.

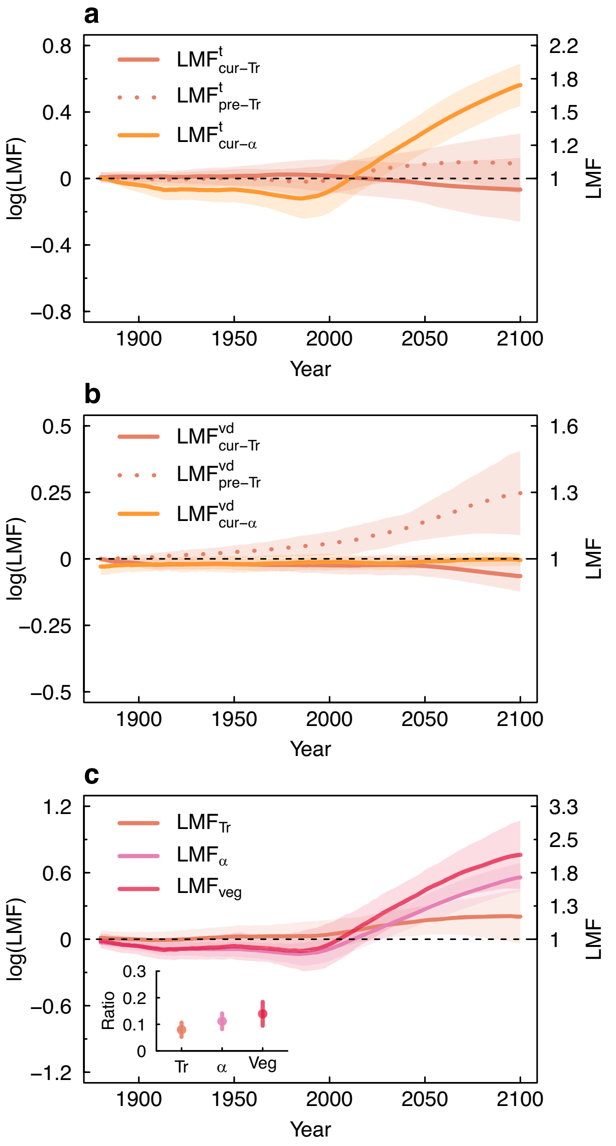

Fig. 2 | Projected vegetation-driven changes in global likelihood of compound soil drought-heat events (LMF) in CMIP6 models. a LMF due to temperature (Ta) and soil moisture (SM) trends related to vegetation biophysics (transpiration (Tr) and albedo (α)) across global vegetated areas. **b** LMF due to Ta and SM variability and dependence related to Tr and α. The subscript “cur” and “pre” represent current and previous seasons, respectively; the superscript “t” and “vd” represent trend and variability&dependency, respectively. **c**, LMF attributed to Tr, α, and both (i.e., $\mathrm{LMF}_{\mathrm{Tr}}$, LMF_{α}, and $\mathrm{LMF}_{\mathrm{Veg}}$), where $\mathrm{LMF}_{\mathrm{Tr}}$ is the sum of $\mathrm{LMF}^{t}_{\mathrm{cur-Tr}}$, $\mathrm{LMF}^{t}_{\mathrm{pre-Tr}}$, $\mathrm{LMF}^{vd}_{\mathrm{cur-Tr}}$ and $\mathrm{LMF}^{vd}_{\mathrm{pre-Tr}}$, LMF_{α} is the sum of $\mathrm{LMF}^{t}_{\mathrm{cur-\alpha}}$ and $\mathrm{LMF}^{vd}_{\mathrm{cur-\alpha}}$, and $\mathrm{LMF}_{\mathrm{Veg}}$ is the sum of $\mathrm{LMF}_{\mathrm{Tr}}$ and LMF_{α}. The inset in (**c**) shows the ratio of $\mathrm{LMF}_{\mathrm{Tr}}$, LMF_{α}, and $\mathrm{LMF}_{\mathrm{Veg}}$ to $\mathrm{LMF}_{\mathrm{Tot}}$ during 2071-2100; $\mathrm{LMF}_{\mathrm{Tot}}$ represents the overall increase in compound soil drought-heat likelihood (i.e., the increase induced by global climate change) (see “methods”). In (**a**–**c**) the solid lines indicate multi-model mean with equal weight, the shaded areas represent ±1 standard deviation across models, and noting that LMF is log transformed and its original values are shown on the right-hand side of the *y*-axis.

heat extremes (Fig. 2a). The trend of Tr from the previous season contributes to an increase in LMF (i.e., $\mathrm{LMF}^{t}_{\mathrm{pre-Tr}}$ steadily increases), while the LMF associated with the Tr trend of the current season (i.e., $\mathrm{LMF}^{t}_{\mathrm{cur-Tr}}$) shows a slight decrease (Fig. 2a) due to the offsetting cooling and drying associated with the current Tr (Supplementary Figs. 2c–f). For the LMF driven by the variability and dependency, only Tr from the previous season ($\mathrm{LMF}^{vd}_{\mathrm{cur-Tr}}$) shows a large positive contribution (Fig. 2b) because of the synergistic effect of previous season Tr on Ta and SM (Supplementary Figs. 2g–h).

Such vegetation-driven changes have a substantial impact on the overall changes in the likelihood of compound soil drought-heat events. In particular, the likelihood is projected to increase by a factor of 2.2 ± 0.6 (i.e., $\mathrm{LMF}_{\mathrm{Veg}}$) by the end of the 21st century (Fig. 2c; primarily attributable to $\mathrm{LMF}^{t}_{\mathrm{cur-\alpha}}$ and $\mathrm{LMF}^{vd}_{\mathrm{pre-Tr}}$, Fig. 2a, b). This increase is equivalent to 13.9 ± 4.5% of the overall increase in compound soil drought-heat likelihood (i.e., the increase induced by global climate change; $\mathrm{LMF}_{\mathrm{Tot}}$) (inset in Fig. 2c). Our results remain robust when we use evapotranspiration instead of transpiration (Supplementary Figs. 3v–x), or employing different moving window lengths (Supplementary Figs. 3g-l), forcing scenarios (Supplementary Figs. 3m–u), and thresholds to define the compound events (Supplementary Figs. 3a–f). They are also robust if we use optimal weight to calculate multi-model means (Supplementary Figs. 4s–u, Methods), or different depths of soil moisture (Supplementary Fig. 4a-i) and initial conditions of model simulations[27,28] (Supplementary Figs. 4j–r). Additionally, the direction of the $\mathrm{LMF}_{\mathrm{Veg}}$ between models is generally consistent across various analyzes (Supplementary Table 1). In particular, the fractional contribution of vegetation to the overall increase in compound event likelihood is similar across various analysis cases, ranging from 12% to 21% across multi-model means (insets in Supplementary Figs. 3–4). However, the magnitude of vegetation-driven LMF intensifies with elevated greenhouse gas emissions (Supplementary Figs. 3m–u), emphasizing the potential of a low-forcing scenario to mitigate vegetation biophysical impacts.

Overall, greening-induced reduction in α, i.e., decreased light reflection, can increase the total energy absorption and warm the land surface[24], but this response is instantaneous and mostly affects the trend component of the LMF for the current season ($\mathrm{LMF}^{t}_{\mathrm{cur-\alpha}}$, Fig. 2a). Tr can cool the surface at a cost of lowered soil moisture levels, hence, its instantaneous effect on Ta and SM is always contradictory[13], resulting in a comparably smaller net effect on LMF. Importantly, Tr changes have sizable time-lagged effects on compound climate in subsequent seasons. When Tr increases for the previous season, its effect on SM will be partially retained and propagated to the current season[18,21]. We show that both the trend and variability of Tr in the previous season dominate the overall effects of Tr on LMF (Fig. 2a-b). Taken together, our analyzes suggest an amplified effect of vegetation biophysics on the global average risk of future compound soil drought-heat events.

Hotspot regions of increasing compound soil drought-heat likelihood

We identify the global hotspots of the projected changes in the compound soil drought-heat likelihood between 30-year historical (1850-1879) and future (2071-2100) periods. The increased likelihood associated with Tr and α (i.e., $\mathrm{LMF}_{\mathrm{Tr}}$ and LMF_{α}) is detected extensively in northern ecosystems (Fig. 3a, b), where $\mathrm{LMF}_{\mathrm{Veg}}$ shows a 5-fold increase (Fig. 3e), equivalent to more than 30% of the overall increase in compound soil drought-heat likelihood due to global change ($\mathrm{LMF}_{\mathrm{Tot}}$, Fig. 3f). $\mathrm{LMF}^{t}_{\mathrm{cur-\alpha}}$ dominates the increased likelihood, contributing to more than 80% of LMF_{α} in those areas, whereas $\mathrm{LMF}^{vd}_{\mathrm{cur-\alpha}}$ exhibits little influence (Figs. 3c and Supplementary Fig. 5). Correspondingly, $\mathrm{LMF}^{vd}_{\mathrm{pre-Tr}}$ is the key driving factor of the likelihood increase in $\mathrm{LMF}_{\mathrm{Tr}}$ (Fig. 3d). Exceptions are found in semi-arid regions around 30°S, where the Tr trend in the warm season ($\mathrm{LMF}^{t}_{\mathrm{cur-Tr}}$) dominates the likelihood increase from Tr, probably because soil moisture memory is weak and vegetation is more reliant on concurrent precipitation[29]. In mid-to-low latitudes, the likelihood of compound soil drought-heat events driven by vegetation ($\mathrm{LMF}_{\mathrm{Veg}}$) shows a decrease in some locations (e.g., eastern South America and central Africa), but there is no consensus in the majority of tropical regions (Fig. 3e). This may be due to an increased α and decreased Tr variability and dependence in these

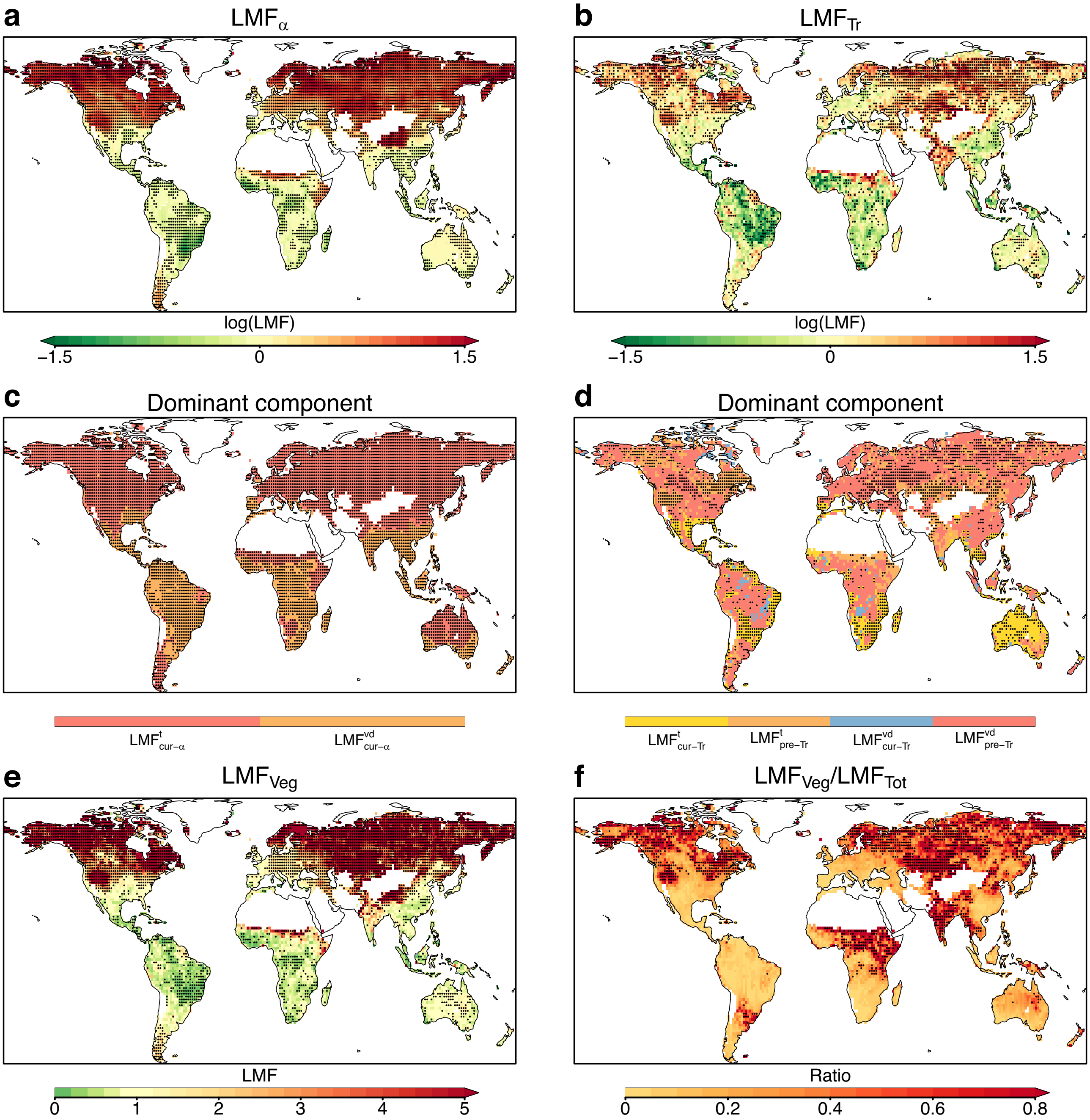

Fig. 3 | Global patterns of projected vegetation-driven changes in the likelihood of compound soil drought-heat event (LMF) in CMIP6 simulations. **a** Multi-model mean of LMF_α during the current season from 2071-2100, relative to the historical (1850-1879) periods. **b** Same as (**a**) but for LMF_{Tr}. **c** Dominant driving components of LMF_α (either $LMF^{t}_{cur-\alpha}$ or $LMF^{vd}_{cur-\alpha}$) that contributes the most to the increase in LMF_α in each grid cell. **d**, Same as **c**, but for LMF_{Tr} encompassing contributions from LMF^{t}_{cur-Tr}, LMF^{t}_{pre-Tr}, LMF^{vd}_{cur-Tr}, and LMF^{vd}_{pre-Tr}. **e** Multi-model mean of LMF_{Veg}, note LMF is presented in its original value. **f** The ratio of LMF_{veg} to LMF_{Tot}. Stippling indicates locations where models project a significant ($P < 0.1$) change in (**a**, **b**, and **e**,) or that more than half of the models show a consistent signal in (**c** and **d**) or the ratio is significantly ($P < 0.1$) larger than 0.2 in (**f**). White land areas are non-vegetated regions.

regions (Supplementary Figs. 6b, g, and l). Our finding remains consistent when using different thresholds for defining compound events, various baseline periods, and different warming scenarios (Supplementary Fig. 5). Furthermore, the magnitude and extent of the corresponding likelihood progressively intensify with rising levels of greenhouse gas emissions during this century (Supplementary Figs. 5i–n). Overall, vegetation contributes substantially to this likelihood increase particularly in northern ecosystems over this century, with the primary contribution from $LMF^{t}_{cur-\alpha}$ and LMF^{vd}_{pre-Tr}.

The dominant role of leaf area in the increasing compound soil drought-heat likelihood

Although Tr and α variation are dominated by vegetation leaf area[23,24], other covarying climatic and environmental factors other than vegetation, such as radiation, vapor pressure deficit, and cloud cover, may also play a role. To elucidate the contribution from vegetation leaf area to LMF, we further explore the physical linkage associated with the two key contributors, i.e., LMF^{vd}_{pre-Tr} and $LMF^{t}_{cur-\alpha}$. To do so, we decompose the associated changes in Tr (or α) into several additive

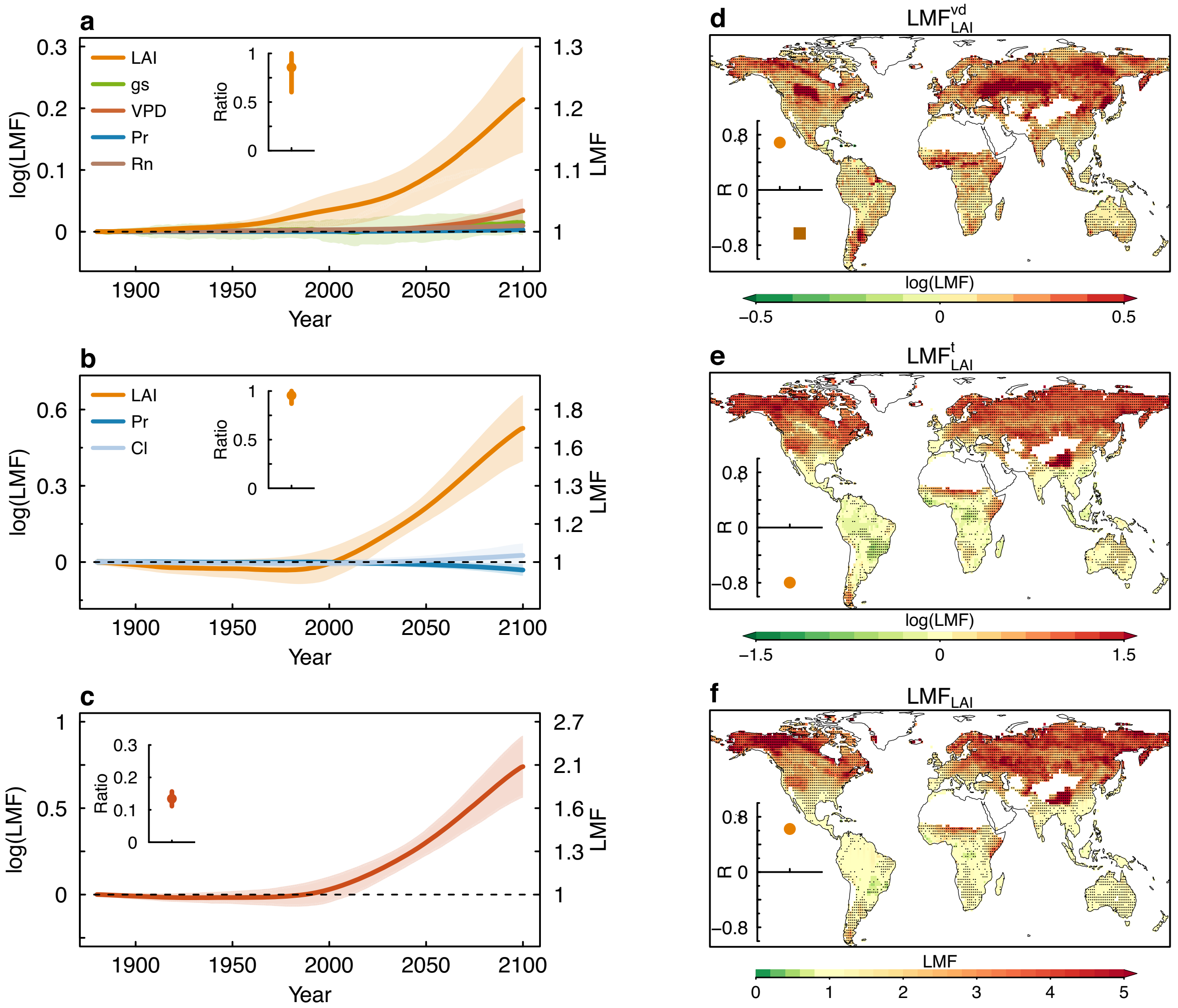

Fig. 4 | Drivers of the changes in the likelihood of compound soil drought-heat event (LMF) associated with vegetation biophysics in CMIP6 models. a Global LMF^{vd}_{pre-Tr} attributed to LAI (i.e., LMF^{vd}_{LAI}), stomatal conductance (gs), vapor pressure deficit (VPD), precipitation (Pr), and net radiation (Rn). **b** Global $LMF^{t}_{cur-\alpha}$ attributed to LAI (i.e., LMF^{t}_{LAI}), Pr, and cloud cover (Cl). **c** Global LMF attributed to LAI (LMF_{LAI}), represented by the summation of LMF^{vd}_{LAI} and LMF^{t}_{LAI}. **d**–**f** The spatial pattern of LMF^{vd}_{LAI} (**d**) LMF^{t}_{LAI} (**e**) and LMF_{LAI} (**f**) between historical (1850-1879) and future periods (2071-2100). The inset in (**a**–**c**) shows the ratio of LMF^{vd}_{LAI} to LMF^{vd}_{pre-Tr} (**a**) LMF^{t}_{LAI} to $LMF^{t}_{cur-\alpha}$ (**b**), and LMF_{LAI} to LMF_{Tot} in future periods (**c**), respectively; LMF is log transformed and its original values are shown on the right-hand side of the *y*-axis. The inset in (**d**-**f**) shows the spatial correlation between LMF^{vd}_{LAI} and LAI-induced variability (orange) /dependence (brown) changes (**d**), LMF^{t}_{LAI} and LAI-induced α changes (**e**), as well as LMF_{LAI} and LMF_{Veg} (**f**), respectively. Stippling in (**d**–**f**) indicates a significant change ($P < 0.1$).

components related to leaf area index (LAI) and other climate factors, followed by the quantification of LMF attributable to LAI and the other factors (see "Methods").

Our results reveal that the projected increase in both LMF^{vd}_{pre-Tr} and $LMF^{t}_{cur-\alpha}$ is predominantly driven by LAI shifts for the corresponding periods (Fig. 4a, b). The aggregate of the two LAI-driven components exhibits a progressive increase during the 21st century, contributing to more than 90% of LMF_{Veg}, equivalent to 13 ± 3.7% of LMF_{Tot} during 2071–2100 (Fig. 4c). Specifically, the additional growth of pre-season LAI is projected to enhance Tr variability and simultaneously intensify the negative dependence of Tr between the pre-season and the warm season (Supplementary Figs. 6a and f). A negative dependence suggests that excessive water extraction during pre-season reduces water availability and inhibits Tr cooling during subsequent warm seasons, thereby increasing the compound soil drought-heat likelihood. Regarding the spatial pattern, the LAI-driven hotspots are also primarily concentrated in the northern ecosystems (Figs. 4d–f), which well ($P < 0.1$) coincided with the most substantial relative increases in LAI (Supplementary Fig. 7). These analyzes highlight the importance of LAI in modulating compound soil drought-heat extremes.

Compound soil drought-heat impact on northern ecosystems

Our analyzes highlight that vegetation-induced changes in compound soil drought-heat extremes are most evident in northern ecosystems. Despite often being considered energy-limited, northern ecosystems can still suffer from these extreme events. For example, we observe a much weaker greening trend in the current season (i.e., peak growing season) than in the previous season (i.e., early growing season) (Fig. 5a). This is also associated with an enhancement of the negative correlation between peak season LAI anomaly and early season LAI anomaly (Fig. 5b), suggesting that the better-than-average early season growth often led to a worse-than-average peak season growth. Both lines of evidence imply that the peak season may be more productive if

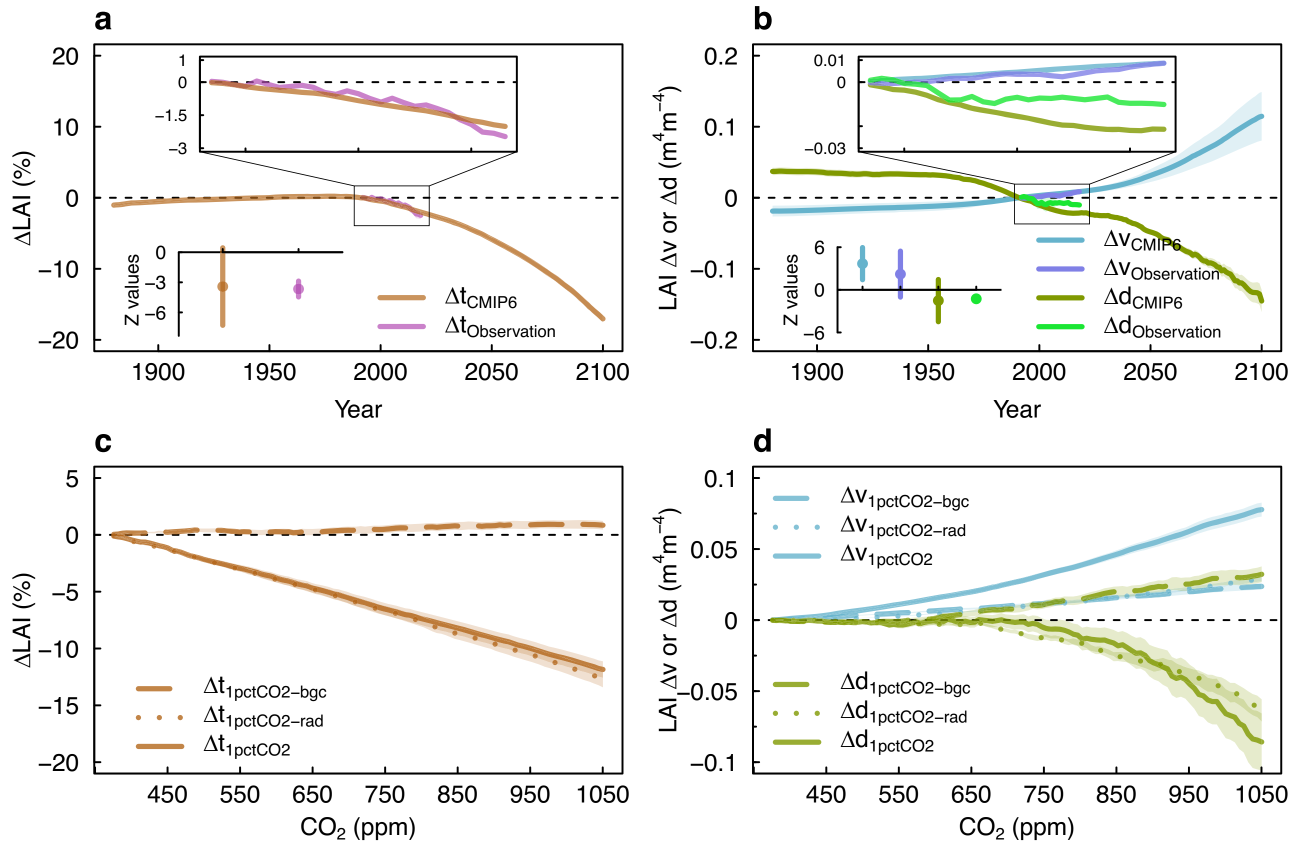

Fig. 5 | Changes in vegetation leaf area index (LAI) across northern ecosystems (> 23° N). **a** The difference of the relative change in LAI (%) between the current and previous seasons. **b** The changes in LAI variability for the current season (Δv, m^4 m^{-4}) and the covariance of LAI (Δd, m^4 m^{-4}) between the previous and current seasons. **c**–**d** Same as (**a**–**b**) but for the three CO_2 experiments. The dependence is represented by covariance, and variability is denoted by variance. Changes in CMIP6 and 1pctCO2 are calculated using a 30-year moving window, while the observed LAI changes from 1982–2018 are computed using a 10-year moving window. For a better comparison between the observed and modeled LAI, the changes in CMIP6 are relative to the baseline of 1963–1992. The lower left inset in (**a**–**b**) shows trends indicated by *Z* values of the Mann-Kendall test, while the upper-middle inset shows a zoom-in during 1992–2018. The shaded areas represent the mean of ±1 standard deviation across models.

compound soil drought-heat extremes do not increase. Additionally, the enhanced compound soil drought-heat risk also jeopardizes the ecosystem stability, as evidenced by increased variability in peak season LAI (Fig. 5b). These results are consistent in both CMIP6 models and satellite observations of LAI, with slight differences in their absolute values.

The magnitude and spatial extent of the LAI-driven increase in the compound likelihood are greater under high emissions scenarios (Supplementary Figs. 8), implying that compound soil drought-heat events are exacerbated by vegetation greening as atmospheric CO_2 concentrations continue to rise. Using ESMs configured with three distinct CO_2 sensitivity experiments (see "Methods"), We further demonstrate that CO_2 radiative effect dominates the increase in compound soil drought-heat extremes (Supplementary Fig. 9), and the associated impact on LAI trend and variability changes in these northern regions (Figs. 5c, d).

Discussion

Our results demonstrate that the greening-induced shifts in land biophysical processes, particularly Tr and α, are expected to increase the global likelihood of compound soil drought-heat events. This is equivalent to 12–21% of the total increment in global compound event likelihood at the end of the 21st century. More than 90% of the projected increases are caused by an increase in the magnitude of LAI and its seasonal dynamics. The enhanced vegetation growth reduces α and triggers additional pre-season Tr increases that further enhance soil moisture depletion and high temperature during the subsequent warm season, amplifying the likelihood of compound extremes. The rise in LAI-induced likelihood is predominantly found in northern ecosystems and is dominated by the indirect response of leaf area to CO_2, suggesting that the CO_2-induced water-saving effect is limited and cannot fully compensate for the warming effect[30,31].

Almost one-fifth of the increase in compound soil drought-heat likelihood is associated with increased vegetation activity in the northern regions. This "greening but warming-drying" phenomenon seems contradictory but can be explained from two perspectives. First, the negative impacts from the compound soil drought-heat extremes may be overridden by the strong positive carryover effect from the previous season. This is supported by a much weaker LAI increase during the peak growing season than the early growing season (Fig. 5a). Second, although compound soil drought-heat extremes have caused a large increase in fire occurrences[32–34] and forest mortality[35,36] in these boreal regions, these changes are most scattered and obscured by the overall greenness increase at coarse spatial resolution[37]. However, these greenness increases contributed by young and fast-growing species are not likely to fully compensate for ecosystem carbon and biodiversity loss. The compound soil drought-heat extremes are likely to decrease ecosystem stability in boreal regions.

Our analysis also highlights the large influence of lagged ecosystem dynamics on the prevalence of compound soil drought-heat extremes. From the pre-season to the warm season, extra water consumption not only leads to lower subsequent soil moisture levels, but the enhanced vegetation growth also increases the water demand[38,39].

When this imbalance between demand and supply accumulates and surpasses the ecosystem carrying capacity, a peculiar type of compound soil drought-heat extreme happens, known as "structural overshoot"[40]. Additionally, such overshoot, when interacting with climate change, can further exacerbate climate events[38,39]. Northern high latitudes have been shown to have the highest likelihood of experiencing structural overshoot drought[18], and our study further projects a much stronger increase in the associated compound extremes in these regions.

The projected increase in compound drought-heat extremes induced by greening has important implications for both ecosystem stability and human wellbeing. Vegetation-driven drought-heat events can have cascading effects on agriculture ecosystems through interactions between plants and various agents in the ecosystem[41–43]. Crops during the critical grain-filling period may also be more frequently affected by drought-heat extremes, both locally due to enhanced early-season growth and remotely through heat advection[44] and water competition[45] from neighboring natural vegetation, potentially jeopardizing global food production. Moreover, in many regions globally with strong vegetation-atmosphere coupling, surface climate conditions are influenced by large-scale atmospheric circulation patterns and local vegetation conditions[14,46]. Our findings emphasize the significance of also considering the pre-existing conditions of vegetation growth in compound event forecasts during the subsequent warm season[18,47].

While our study focuses on natural ecosystems, these insights are relevant for nature-based solutions in urban environment. This is due to the consistent effects of vegetation on climate at both macro and micro scales, particularly through mechanisms such as modifications of albedo and transpiration[13,48]. Urban green initiatives can mitigate urban heat by enhancing albedo and transpiration, especially in mid-to-low latitudes[49,50]. Consistently, we show that vegetation greening will mitigate compound soil drought-heat in these regions, implying potential climate benefits from nature-based solutions in urban settings. Conversely, in high-latitude or arid regions, urban greening might not yield the expected benefits, likely due to the projected exacerbation of dry and heat extremes by climate change and urban development[51,52]. Whether urban greening can mitigate the compound soil drought-heat extremes also depends on human management practices, such as irrigation and species selections, and faces large uncertainties in model simulations. Therefore, effective future urban climate mitigation efforts should incorporate high-resolution modeling and delicate management to ensure the success of these interventions in the face of ongoing climate change.

Compound soil drought-heat extremes may disproportionately impact the global carbon cycle compared to univariate extremes, not only through the direct effect on vegetation photosynthesis, but through other processes including enhanced fire emission[53], permafrost thaw[54], variation in boundary layer[55], and the complex positive interactions therein[56]. However, these processes lack robust observational constraints and are still not well-represented in the state-of-the-art models, contributing to the uncertainties in future global compound soil drought-heat extremes predictions. Our global quantification of the effects of vegetation fingerprint on compound soil drought-heat events emphasizes the importance of accurately representing land processes for future projections of compound extremes, and motivates the need to incorporate vegetation biophysics into climate decision-making and adaptation strategies related to compound extremes.

Methods

CMIP6 model simulations

We used outputs from 17 state-of-the-art ESMs that participate in CMIP6 (Supplementary Table 2). We use CMIP6 models since a lengthy time series is necessary to acquire an adequeate number of samples for estimating compound event likelihood, and evaluate its trend attributed to vegetation changes[8,22,26,28]. Remote sensing observations are limited in temporal coverage and do not have the capability to predict the changes of compound extremes in the future. Moreover, our analyzes (Supplementary Fig. 10) and ample evidence suggest that the overall trends in historical drought[57–59], temperature[60–62], and vegetation characteristics[13,63] (such as LAI, transpiration, and others) simulated by the ESMs are generally consistent with observations. The various output variables from this consistent modeling framework also allow us to reliably investigate the underlying processes and mechanisms driving such changes. Hence, we utilize ESMs from CMIP6, which integrate the latest human understanding of knowledge on various land surface processes[25], to project the vegetation-driven compound soil drought-heat likelihood.

The selected CMIP6 models all report the required variables and incorporate the dynamic responses of stomatal conductance and vegetation cover to climate change and increased CO_2. We used monthly total soil moisture (mrso), near-surface air temperature (tas), transpiration (tran), evapotranspiration (evspsbl), runoff (mrro), precipitation (pr), relative humidity (hurs), leaf area index (lai), sensible heat flux (hfss), latent heat flux (hfls), total cloud cover percentage (clt), surface downwelling shortwave radiation (rsds), and surface upwelling shortwave radiation (rsus) from the historical (1850-2014), SSP1-2.6, SSP2-4.5, SSP3-7.0, and SSP5-8.5 (2015-2100) simulations. Surface albedo (α) was computed as the ratio of rsus to rsds. From CanESM5, CanESM5-1, and MPI-ESM1-2-LR, we extracted all ensemble members (i.e., 50, 20, and 20), respectively, to assess the effect of initial conditions on the estimated compound soil drought-heat likelihood. Relative humidity was not available for the BCC-CSM2-MR, and was calculated from specific humidity, near-surface air pressure, and Ta. Considering the divergent depth of soil moisture across model[64,65], multiple layer soil moisture (mrsol) is also used to obtain surface SM and SM at 1 m and 2 m. We linearly interpolate the profiles of each model and then extract the soil moisture at 1 m and 2m[66]. The satellite LAI are from GIMMS LAI3g[67] and GLASS LAI[68]. We also used three idealized single-forcing CMIP6 experiments (i.e., 1pctCO2, 1pctCO2-rad and 1pctCO2-bgc) that participate in the coupled carbon-climate ESMs[69]. In these experiments, the influence of atmospheric CO_2 was separated into the radiation effect and vegetation physiological effect. In 1pctCO2, both the atmospheric and land surface modules experience a 1% annual increase of atmospheric CO_2 starting from 280 ppm (pre-industrial) to 1140 ppm ($4 \times CO_2$) over a 140-year period. The rate of CO_2 increase is similar to that in historical and SSP5-8.5 simulations. In 1pctCO2-bgc, only the vegetation module experiences the increase in CO_2, while the atmosphere continuously experiences pre-industrial CO_2 levels. By contrast, in 1pctCO2-rad, only the atmospheric module is subjected to the increase in CO_2, while the vegetation module is set to a fixed CO_2 concentration at the pre-industrial level. These simulations have been commonly used to investigate the impact of CO_2 radiative and physiological effects on climate extremes[31,66,70]. Ten climate models that participated in the three idealized single-forcing CMIP6 (Supplementary Table 2) were used. In these simulations, we also used the above-mentioned monthly outputs. All the model outputs utilized in this study were resampled to a common spatial resolution of 1.5° × 1.5° by using bilinear interpolation.

A framework for quantifying the likelihood of compound soil drought-heat events from vegetation biophysics

The total LMF. Compound soil drought-heat extremes are expected to have large impacts on natural ecosystems and human society, especially for those happen during the warm season. Additionally, the warm season also overlaps with the main growing season for most regions, during which vegetation change through modifying α and Tr can substantially regulate SM and Ta[13,21]. We thus focus on global vegetated regions during the warm season. Following ref. 26, the warm season is defined as the average hottest three consecutive months during study periods in each model grid cell.

Following ref. 26, we used the likelihood multiplication factor (LMF) to quantify the change in the frequency of compound soil drought-heat events driven by Ta and SM (hereafter referred to as $\mathrm{LMF_{Tot}}$). We first employed the commonly used bivariate copulas to calculate the joint probability of a compound soil drought-heat event. Accordingly, our two variables are monthly Ta and the opposite of SM (-SM) over the warm season. Given two random variables X (i.e., Ta) and Y (i.e., -SM), the joint probability distribution function of X and Y with a copula C can be expressed as

$$\mathrm{F}(x, y) = \mathrm{P}(X \le x, Y \le y) = \mathrm{C}(u, v) \tag{1}$$

Where P is the joint cumulative probability; u and v are the uniform distribution of X and Y, respectively. The joint probability of a compound soil drought-heat event during the historical period, defined by both variables exceeding their specific thresholds, can be expressed as

$$\mathrm{p_{his}} = \mathrm{P_{his}}\left(u > \mathrm{u_{his}} \bigcap v > \mathrm{v_{his}}\right) = 1 - \mathrm{u_{his}} - \mathrm{v_{his}} + \mathrm{C_{his}}(\mathrm{u_{his}}, \mathrm{v_{his}}) \tag{2}$$

where $\mathrm{C_{his}}$ is the copula during the historical period. $\mathrm{u_{his}}$ and $\mathrm{v_{his}}$ are Ta and SM thresholds, respectively, and both are set at 0.9, which is a common threshold to define climate extremes.

Subsequently, we calculated the future thresholds of X and Y, corresponding to the 90th quantile values during the historical period. For example, future thresholds of X ($\mathrm{u_{fut}}$) can be expressed as

$$\mathrm{u_{fut}} = \mathrm{F_{fut}}\left(\mathrm{X_{90-his}}\right) \tag{3}$$

Where $X_{90\text{-his}}$ is the 90th percentile value of X during the historical period, $\mathrm{F_{fut}}$ is the normal cumulative distribution function (CDF) of X during the future period. We then recomputed a new copula driven by future X and Y, and used Eq. (2) to calculate the future joint probability ($\mathrm{p_{fut}}$). The $\mathrm{LMF_{Tot}}$ is defined as the ratio of $\mathrm{p_{fut}}$ to $\mathrm{p_{his}}$

$$\mathrm{LMF_{Tot}} = \frac{\mathrm{p_{fut}}}{\mathrm{p_{his}}} \tag{4}$$

An increase in likelihood is indicated by a value greater than one. We used the function "BiCopCDF" in R VineCopula package[71] to calculate the joint probability.

The decomposition of LMF. Following ref. 22, changes in trend, variability, and dependence of relevant drivers can affect the likelihood of all types of compound events. For example, an increase (reduction) in Ta (SM), an escalation in variability, or an intensification of negative dependence between Ta and SM can increase the compound event likelihood[22]. We partition $\mathrm{LMF_{Tot}}$ into components attributed to Ta trend, SM trend, variability, and dependence.

We first calculated the LMF attributed to changes in variability (referred to as $\mathrm{LMF^{v}_{Tot}}$). Using Eq. (3), but with the CDF that fixes the mean values of Ta (SM) in accordance with the historical period while allowing standard deviation to change, we calculated the future Ta (SM) threshold (i.e., $\mathrm{u^{v-Ta}_{fut}}$ and $\mathrm{v^{v-SM}_{fut}}$, where the superscript v stands for variability). With this, we obtained the joint probability only encompassing information on the variability of Ta and SM ($\mathrm{p^{v}_{fut}}$). $\mathrm{LMF^{v}_{Tot}}$ is given by

$$\mathrm{p^{v}_{fut}} = \mathrm{P_{fut}}\left(\mathrm{u} > \mathrm{u^{v-Ta}_{fut}} \bigcap \mathrm{v} > \mathrm{u^{v-SM}_{fut}}\right) = 1 - \mathrm{u^{v-Ta}_{fut}} - \mathrm{u^{v-SM}_{fut}} + \mathrm{C_{fut}}\left(\mathrm{u^{v-Ta}_{fut}}, \mathrm{u^{v-SM}_{fut}}\right) \tag{5}$$

$$\mathrm{LMF^{v}_{Tot}} = \frac{\mathrm{p^{v}_{fut}}}{\mathrm{p_{fut}}} \tag{6}$$

Where $\mathrm{C_{fut}}$ is the newly recalculated copula driven by future Ta and SM. We then calculated the LMF related to trends in Ta and SM (i.e., $\mathrm{LMF^{t-Ta}_{Tot}}$ and $\mathrm{LMF^{t-SM}_{Tot}}$), using Ta as an example. We derived a new Ta threshold ($\mathrm{u^{t-v-Ta}_{fut}}$), employing a CDF calculated from future Ta which contains both changes in mean and variability of Ta. We then obtained the joint probability containing information on Ta's variability and trend ($\mathrm{p^{t-v-Ta}_{fut}}$), by setting the threshold for SM to 0.9, as well as the joint probability for Ta's variability only ($\mathrm{p^{v-Ta}_{fut}}$). The $\mathrm{LMF^{t-Ta}_{Tot}}$ is given by

$$\mathrm{p^{t-v-Ta}_{fut}} = \mathrm{P_{fut}}\left(\mathrm{u} > \mathrm{u^{t-v-Ta}_{fut}} \bigcap \mathrm{v} > 0.9\right) = 1 - \mathrm{u^{t-v-Ta}_{fut}} - 0.9 + \mathrm{C_{fut}}\left(\mathrm{u^{t-v-Ta}_{fut}}, 0.9\right) \tag{7}$$

$$\mathrm{p^{v-Ta}_{fut}} = \mathrm{P_{fut}}\left(\mathrm{u} > \mathrm{u^{v-Ta}_{fut}} \bigcap \mathrm{v} > 0.9\right) = 1 - \mathrm{u^{v-Ta}_{fut}} - 0.9 + \mathrm{C_{fut}}\left(\mathrm{u^{v-Ta}_{fut}}, 0.9\right) \tag{8}$$

$$\mathrm{LMF^{t-Ta}_{Tot}} = \frac{\mathrm{p^{t-v-Ta}_{fut}}}{\mathrm{p^{v-Ta}_{fut}}} \tag{9}$$

The LMF changes resulting from SM's trend can be calculated in a similar way. To quantify the LMF due to dependence changes ($\mathrm{LMF^{d}_{Tot}}$), we set future thresholds ($\mathrm{u^{d-Ta}_{fut}}$, $\mathrm{v^{d-SM}_{fut}}$) being 90th quantile for both SM and Ta based on model prediction for future period, and used the Eq. (2) and $\mathrm{C_{fut}}$ to obtain the future joint probability due to shifts in dependence ($\mathrm{p^{d}_{fut}}$). $\mathrm{LMF^{d}_{Tot}}$ is given by

$$\mathrm{LMF^{d}_{Tot}} = \frac{\mathrm{p^{d}_{fut}}}{\mathrm{p_{his}}} \tag{10}$$

Since $\mathrm{LMF_{Tot}}$ is overall driven by changes in trend, variability and dependence[22], it can also be calculated from the as the summation of the individual components after logarithm transformed:

$$\log(\mathrm{LMF_{Tot}}) = \log(\mathrm{LMF^{t-SM}_{Tot}}) + \log(\mathrm{LMF^{t-Ta}_{Tot}}) + \log(\mathrm{LMF^{v}_{Tot}}) + \log(\mathrm{LMF^{d}_{Tot}}) \tag{11}$$

In particular, we find a very high consistency between $\log(\mathrm{LMF_{Tot}})$ estimated from Eq. (4) and the summation of all components in Eq. (11) (Supplementary Fig. 11). Additionally, $\log(\mathrm{LMF_{Tot}})$ and the summation exhibit good spatial consistency at a global scale. These analyzes suggest that our decomposition method is in line with theoretical principles.

The changes in each individual LMF component predominantly stem from the anomalies of the respective element. For example, $\mathrm{LMF^{t-SM}_{Tot}}$ is caused by shifts in SM trends, and $\mathrm{LMF^{v}_{Tot}}$ is caused by changes in the product of Ta and SM standard deviation. To establish the relationship between LFM components and the variability characteristics (trend, variation, dependency) of the two variables, we computed each individual LMF component for each consecutive 30-year period from 1850–2100, in relation to the first 30-year period (1850-1879) within each model grid cell (a total of 221 points). We then build a piecewise function to predict each LMF component (after log-transformation) from Ta and SM variability characteristics using the function "segmented.lm" in R package "segmented"[72].

Ta and SM changes associated with Tr and α. Tr is expected to affect both Ta and SM simultaneously[24,73,74]. Additionally, evidence from observations and models also indicates lagged effects of spring Tr on summer SM[20,75–77], such as increased summer drying due to enhanced spring Tr[21]. Moreover, the change in α can also regulate the land energy balance and further affect Ta. We incorporated changes in trend, variability, and dependence of SM and Ta from Tr of the previous season and current season, and the associated changes due to current α (Supplementary Figs. 2a,b).

Given the additive nature of the log(LMF), we performed separate calculations for each pertinent item related to Tr and α. Following refs. [14,78], we applied the surface energy balance equation to assess the impact of changes in Tr and α on Ta. Briefly, changes in Tr can modify the surface energy budget and alter land surface temperature, further warming or cooling the local Ta. The surface energy balance equation is given by

$$S_{in}(1-\alpha)+\varepsilon_s\sigma\left(\varepsilon_a Ta^4 - Ts^4\right)=\lambda(Tr+Ei+Es)+H+G \tag{12}$$

Where S_{in} represents surface downward shortwave radiation, λ is the latent heat of vaporization, Ei is canopy evaporation, Es is soil evaporation, H is sensible heat flux, and G is ground heat flux. ε_s, σ, ε_a, and Ts denote land surface emissivity, Stephan-Boltzmann constant, atmospheric air emissivity, and land surface temperature, respectively.

By differentiating Eq. (12), we obtained the sensitivity of Ta to Tr (i.e., $\frac{\delta Ta}{\delta Tr}$), and calculated the effect of changes in Tr's trend on Ta (Δt^{Ta}_{cur-Tr}).

$$\Delta t^{Ta}_{cur-Tr}=\frac{\delta Ta}{\delta Tr}\left(Tr^{fut}-Tr^{his}\right) \tag{13}$$

Where Tr^{fut} and Tr^{his} denote the average of Tr during historical and future periods. Similarly, combing the sensitivity of Ta to α from Eq. (12) (i.e., $\frac{\delta Ta}{\delta \alpha}$) and the long-term α trends, we obtained the effect of changes in α's trend on Ta ($\Delta t^{Ta}_{cur-\alpha}$).

As for SM, we need to consider both Tr of current period (*k*) and previous period (*k-1*). We used a simple water balance equation to characterize the impact of Tr on SM. The water balance equation is given by

$$SM_k=SM_{k-1}+Pr_{k-1}-Tr_{k-1}-Q_{k-1} \tag{14}$$

Where SM_k is SM at time *k*. SM_{k-1}, Pr_{k-1}, Tr_{k-1}, and Q_{k-1} are the average SM, precipitation, Tr, and runoff from the previous three months, respectively. Using three-month average values can consider the potential collective effects of spring vegetation water use and longer timescales of droughts[75]. Due to the different surface and climate characteristics, the effect of Tr_{k-1} to SM_k can be different across grid cells. For example, in very wet regions with abundant precipitation, water losses from Tr will be fully replenished, and will have little effect on SM. We therefore build a linear model for each grid cell to quantify the sensitivity of SM to Tr (i.e., $\frac{\delta SM}{\delta Tr}$) using observations from both historical and future periods. If we consider the precipitation events as randomly occurring, such a sensitivity can also be applied to calculate the effect of current Tr on SM. With this, the SM changes due to the trend of warm season Tr (Δt^{SM}_{cur-Tr}) can be calculated as:

$$\Delta t^{SM}_{cur-Tr}=\frac{\delta SM}{\delta Tr}\left(Tr^{fut}_k-Tr^{his}_k\right) \tag{15}$$

The Eq. (15) can also be used to calculate the SM changes due to trend of previous season (Δt^{SM}_{pre-Tr}) using Tr_{k-1} from historical and future periods. We then calculated the antecedent and current effects of a Tr anomaly (Tr_{ano}) on dependence using both $\frac{\delta SM}{\delta Tr}$ estimated from Eq. (14) and $\frac{\delta Ta}{\delta Tr}$ estimated from Eq. (12):

$$\Delta d_{cur-Tr}=cov\left(\frac{\delta SM}{\delta Tr}Tr^{v,fut}_k,\frac{\delta Ta}{\delta Tr}Tr^{v,fut}_k\right)-cov\left(\frac{\delta SM}{\delta Tr}Tr^{v,his}_k,\frac{\delta Ta}{\delta Tr}Tr^{v,his}_k\right) \tag{16}$$

$$\Delta d_{pre-Tr}=cov\left(\frac{\delta SM}{\delta Tr}Tr^{v,fut}_{k-1},\frac{\delta Ta}{\delta Tr}Tr^{v,fut}_k\right)-cov\left(\frac{\delta SM}{\delta Tr}Tr^{v,his}_{k-1},\frac{\delta Ta}{\delta Tr}Tr^{v,his}_k\right) \tag{17}$$

Where cov is the covariance that quantifies the direction and magnitude of dependence between two variables. Δd_{cur-Tr} represents dependence change due to current Tr_{ano}, while Δd_{pre-Tr} denotes changes in dependence between SM (caused by preseason Tr_{ano}) and Ta (caused by current Tr_{ano}). $Tr^{v,his}_k$ and $Tr^{v,fut}_k$ are monthly Tr_{ano} at time k during historical and future periods, respectively. $Tr^{v,his}_{k-1}$ and $Tr^{v,fut}_{k-1}$ was calculated by averaging monthly Tr_{ano} from time *k-1* to *k-3* during historical and future periods, respectively.

We finally calculated the changes in variability related to Tr. The Tr-driven change in variability is defined as the products between Tr-driven Ta and SM anomalies, given that LMF^{v}_{Tot} is driven by changes in the product of Ta and SM standard deviation (see following section), and this definition facilitates the comparison with LMF pairs related to Tr-driven variability and dependence.

$$\Delta v_{cur-Tr}=sd\left(\frac{\delta SM}{\delta Tr}Tr^{v,fut}_k\right)sd\left(\frac{\delta Ta}{\delta Tr}Tr^{v,fut}_k\right)-sd\left(\frac{\delta SM}{\delta Tr}Tr^{v,his}_k\right)sd\left(\frac{\delta Ta}{\delta Tr}Tr^{v,his}_k\right) \tag{18}$$

$$\Delta v_{pre-Tr}=sd\left(\frac{\delta SM}{\delta Tr}Tr^{v,fut}_{k-1}\right)sd\left(\frac{\delta Ta}{\delta Tr}Tr^{v,fut}_{k-1}\right)-sd\left(\frac{\delta SM}{\delta Tr}Tr^{v,his}_{k-1}\right)sd\left(\frac{\delta Ta}{\delta Tr}Tr^{v,his}_{k-1}\right) \tag{19}$$

Where sd denotes standard deviation. Δv_{cur-Tr} represents the variability change due to current Tr_{ano}, while Δv_{pre-Tr} denotes the variability change induced by preseason and current Tr_{ano}. Using the Eqs. (16 and 18) and considering the changes in Ta variability associated with α, we obtained changes in variability and dependence induced by α anomalies (i.e., $\Delta v_{cur-\alpha}$ and $\Delta d_{cur-\alpha}$):

$$\Delta v_{cur-\alpha}=sd\left(\frac{\delta SM}{\delta Tr}Tr^{v,fut}_k\right)sd\left(\frac{\delta Ta}{\delta \alpha}\alpha^{v,fut}_k\right)-sd\left(\frac{\delta SM}{\delta Tr}Tr^{v,his}_k\right)sd\left(\frac{\delta Ta}{\delta \alpha}\alpha^{v,his}_k\right) \tag{20}$$

$$\Delta d_{cur-\alpha}=cov\left(\frac{\delta SM}{\delta Tr}Tr^{v,fut}_k,\frac{\delta Ta}{\delta \alpha}\alpha^{v,fut}_k\right)-cov\left(\frac{\delta SM}{\delta Tr}Tr^{v,his}_k,\frac{\delta Ta}{\delta \alpha}\alpha^{v,his}_k\right) \tag{21}$$

The LMF caused by changes in Tr and α. In the previous sections, we calculated the LMF and its components related to the trend, variability, and dependence of Ta and SM. We employed a piecewise regression function to characterize these relationships for each model and for each grid cell. We also used energy balance equations and water balance equations to quantify the changes in Ta and SM trend, variability and dependence associated with Tr and α. With these, we can use the "chain rule" to calculate the changes in Tr and α and their contribution to LMF, i.e., LMF from Δt^{Ta}_{cur-Tr} and Δt^{SM}_{cur-Tr} (LMF^{t-Ta}_{cur-Tr} and LMF^{t-SM}_{cur-Tr}), $\Delta d_{cur\text{-}Tr}$ and $\Delta v_{cur\text{-}Tr}$ (LMF^{d}_{cur-Tr} and LMF^{v}_{cur-Tr}), $\Delta d_{pre\text{-}Tr}$ and $\Delta v_{pre\text{-}Tr}$ (LMF^{d}_{pre-Tr} and LMF^{v}_{pre-Tr}), $\Delta d_{cur\text{-}\alpha}$ and $\Delta v_{cur\text{-}\alpha}$ ($LMF^{d}_{cur-\alpha}$ and $LMF^{v}_{cur-\alpha}$), $\Delta t^{Ta}_{cur-\alpha}$ ($LMF^{t}_{cur-\alpha}$), and Δt^{SM}_{pre-Tr} (LMF^{t-Ta}_{cur-Tr}). For example, LMF^{t-Ta}_{cur-Tr} is given by

$$\log\left(LMF^{t-Ta}_{cur-Tr}\right)=f_{t-Ta}\left(\Delta t^{Ta}_{cur-Tr}\right) \tag{22}$$

Where f_{t-Ta} denotes the piecewise function formulated by $\log(LMF^{t-Ta}_{Tot})$ and the change in Ta's trend.

To assess the impacts of the current Tr trend on compound event likelihood, we added LMF^{t-Ta}_{cur-Tr} and LMF^{t-SM}_{cur-Tr} to get LMF^{t}_{cur-Tr}. Given that Tr-driven (or α-driven) variability and dependence are quantified by variance and covariance, respectively, and are therefore compatible, we combined the $\mathrm{LMF}^{v}_{cur-Tr}$ and $\mathrm{LMF}^{d}_{cur-Tr}$ ($\mathrm{LMF}^{vd}_{cur-Tr}$), $\mathrm{LMF}^{v}_{pre-Tr}$ and $\mathrm{LMF}^{d}_{pre-Tr}$ ($\mathrm{LMF}^{vd}_{pre-Tr}$), $\mathrm{LMF}^{v}_{cur-\alpha}$ and $\mathrm{LMF}^{d}_{cur-\alpha}$($\mathrm{LMF}^{vd}_{cur-\alpha}$), to represent the influences of variability and dependence on compound event likelihood. We set any the modeled log(LMF) values larger (smaller) than 4.6 (−4.6) to missing (a very small proportion, 0.29%), given that log(LMF_{Tot}) is generally less than 4.6 (its value before logarithmic transformation is 100)[6,26]. Our evaluation shows that the prediction model satisfactorily captures the linkage between response and predictive variables (Supplementary Figs. 12). Specifically, the simulation and observation exhibit satisfactory correlation alongside minimal error, and present strong spatial consistency across a global scale.

We tested whether the ensemble median of the models shows a change in likelihood with the one-sided sign test[26]. We highlighted regions for which the model ensemble median of the LMF is significantly larger than or less than 0 with stippling. Global statistics such as means and quantiles are based on the arithmetic mean for a balanced reflection of the frequency of events, since LMF represents the frequency of compound events independent of the area size[6,8,26].

The contribution of LAI in Tr- and α- driven LMF. Changes in Tr_{ano} can be linked to factors such as leaf area index (LAI), precipitation (Pr), net radiation (Rn), stomatal conductance (gs), and vapor pressure deficit (VPD). Following ref.[79], we used a multivariate regression framework to investigate the Tr_{ano} associated with these factors. This approach adeptly factors out the direct impacts of alterations in climatic and vegetation factors on terrestrial energy fluxes[79] and can be consistently applied to various ESM outputs[80]. Partial least-squares regression was used to overcome the potential multicollinearity problem of drivers for each model grid cell and each month[81]. The Tr_{ano} was expressed as

$$\mathrm{Tr}_{ano} = \frac{\delta \mathrm{Tr}_{ano}}{\delta \mathrm{LAI}}\mathrm{LAI} + \frac{\delta \mathrm{Tr}_{ano}}{\delta \mathrm{gs}}\mathrm{gs} + \frac{\delta \mathrm{Tr}_{ano}}{\delta \mathrm{Rn}}\mathrm{Rn} + \frac{\delta \mathrm{Tr}_{ano}}{\delta \,\mathrm{Pr}}\mathrm{Pr} + \frac{\delta \mathrm{Tr}_{ano}}{\delta \mathrm{VPD}}\mathrm{VPD} \tag{23}$$

Where LAI, gs, Rn, Pr and VPD are detrended and deseasonalized sequences. VPD was calculated from Ta and relative humidity. gs was estimated by Tr per leaf area following ref.[82]. We calculated the changes in the corresponding variability and dependence (i.e., Δv and Δd), and subsequently obtained Δv attributed to LAI, gs, VPD, Pr, and Rn, as well as Δd attributed to these factors. Combining these factors with the above framework, we further partition $\mathrm{LMF}^{vd}_{pre-Tr}$ associated with LAI (LMF^{vd}_{LAI}), gs, VPD, Pr, and Rn. We also employed the consistent methods to calculate the change in α's trend associated with LAI, Pr, and Cl, as well as partition $\mathrm{LMF}^{t}_{cur-\alpha}$ related to LAI (LMF^{t}_{LAI}) and other factors.

Our evaluation shows that this approach can effectively replicate the correctly associated changes in Tr and α at the global scale (Supplementary Fig. 13). This calculation was conducted for each consecutive 30-year period from 1851 to 2100, relative to the first 30-year period (1850-1879) within each model grid cell. We utilized the pls R packages to execute the partial least-squares regression. In the three CO_2 sensitivity experiments, we assessed the changes in LAI between the first (years 1-30) and last (years 111-140) 30-year periods, and performed a similar analysis to separate the effect of LAI on Tr_{ano} and α.

Data availability

The original CMIP6 model simulations are publicly available from the CMIP6 data portal (https://esgf-node.llnl.gov/search/cmip6/). Earth system models and simulations used in this study are listed in Supplementary Table 1. The data generated in this study are provided in the Source Data file (https://doi.org/10.6084/m9.figshare.27889785.v1). Source data are provided with this paper.

Code availability

The code used for the calculation of Tr- and α-induced LMF is available at GitHub (https://github.com/jlyfine/comveg), and have been archived on figshare (https://doi.org/10.6084/m9.figshare.27889749.v1)

References

1. Zscheischler, J. et al. Impact of large-scale climate extremes on biospheric carbon fluxes: an intercomparison based on MsTMIP data. *Glob. Biogeochemical Cycles* **28**, 585–600 (2014).
2. Grumm, R. H. The central european and russian heat event of july–august 2010. *Bull. Am. Meteorological Soc.* **92**, 1285–1296 (2011).
3. Gampe, D. et al. Increasing impact of warm droughts on northern ecosystem productivity over recent decades. *Nat. Clim. Chang.* **11**, 772–779 (2021).
4. Li, J. et al. Hydroclimatic extremes contribute to asymmetric trends in ecosystem productivity loss. *Commun. Earth Environ.* **4**, 1–10 (2023).
5. Yin, J. et al. Future socio-ecosystem productivity threatened by compound drought–heatwave events. *Nat. Sustain* **6**, 259–272 (2023).
6. Zhou, S., Zhang, Y., Park Williams, A. & Gentine, P. Projected increases in intensity, frequency, and terrestrial carbon costs of compound drought and aridity events. *Sci. Adv.* **5**, eaau5740 (2019).
7. Mukherjee, S. & Mishra, A. K. Increase in compound drought and heatwaves in a warming world. *Geophys. Res. Lett.* **48**, e2020GL090617 (2021).
8. Zhou, S., Yu, B. & Zhang, Y. Global concurrent climate extremes exacerbated by anthropogenic climate change. *Sci. Adv.* **9**, eabo1638 (2023).
9. Alizadeh, M. R. et al. A century of observations reveals increasing likelihood of continental-scale compound dry-hot extremes. *Science Advances* **6**, eaaz4571 (2020).
10. Qing, Y., Wang, S., Yang, Z.-L. & Gentine, P. Soil moisture–atmosphere feedbacks have triggered the shifts from drought to pluvial conditions since 1980. *Commun Earth Environ* **4**, 1–10 (2023).
11. Zhou, S. et al. Land–atmosphere feedbacks exacerbate concurrent soil drought and atmospheric aridity. *Proc. Natl Acad. Sci.* **116**, 18848–18853 (2019).
12. Bastos, A. et al. A joint framework for studying compound ecoclimatic events. *Nat. Rev. Earth Environ.* **4**, 333–350 (2023). (2023).
13. Piao, S. et al. Characteristics, drivers and feedbacks of global greening. *Nat. Rev. Earth Environ.* **1**, 14–27 (2020).
14. Zeng, Z. et al. Climate mitigation from vegetation biophysical feedbacks during the past three decades. *Nat. Clim. Change* **7**, 432–436 (2017).
15. Li, Y. et al. Biophysical impacts of earth greening can substantially mitigate regional land surface temperature warming. *Nat. Commun.* **14**, 121 (2023).
16. Wu, J. et al. Earth greening mitigates hot temperature extremes despite the effect being dampened by rising CO2. *One Earth* **7**, 100–109 (2024).
17. Forzieri, G., Alkama, R., Miralles, D. G. & Cescatti, A. Satellites reveal contrasting responses of regional climate to the widespread greening of Earth. *Science* **356**, 1180–1184 (2017).
18. Zhang, Y., Keenan, T. F. & Zhou, S. Exacerbated drought impacts on global ecosystems due to structural overshoot. *Nat. Ecol. Evol.* **5**, 1490–1498 (2021).
19. Mankin, J. S., Seager, R., Smerdon, J. E., Cook, B. I. & Williams, A. P. Mid-latitude freshwater availability reduced by projected vegetation responses to climate change. *Nat. Geosci.* **12**, 983–988 (2019).
20. Wolf, S. et al. Warm spring reduced carbon cycle impact of the 2012 US summer drought. *Proc. Natl Acad. Sci.* **113**, 5880–5885 (2016).

21. Lian, X. et al. Summer soil drying exacerbated by earlier spring greening of northern vegetation. *Sci. Adv.* **6**, eaax0255 (2020).
22. Zscheischler, J. et al. A typology of compound weather and climate events. *Nat. Rev. Earth Environ.* **1**, 333–347 (2020).
23. Bonan, G. B. Forests and climate change: forcings, feedbacks, and the climate benefits of forests. *Science* **320**, 1444–1449 (2008).
24. Alkama, R. & Cescatti, A. Biophysical climate impacts of recent changes in global forest cover. *Science* **351**, 600–604 (2016).
25. Eyring, V. et al. Overview of the Coupled Model Intercomparison Project Phase 6 (CMIP6) experimental design and organization. *Geoscientific Model Dev.* **9**, 1937–1958 (2016).
26. Zscheischler, J. & Seneviratne, S. I. Dependence of drivers affects risks associated with compound events. *Sci. Adv.* **3**, e1700263 (2017).
27. Bevacqua, E., Zappa, G., Lehner, F. & Zscheischler, J. Precipitation trends determine future occurrences of compound hot–dry events. *Nat. Clim. Chang.* **12**, 350–355 (2022).
28. Bevacqua, E. et al. Advancing research on compound weather and climate events via large ensemble model simulations. *Nat. Commun.* **14**, 2145 (2023).
29. Miguez-Macho, G. & Fan, Y. Spatiotemporal origin of soil water taken up by vegetation. *Nature* **598**, 624–628 (2021).
30. Keenan, T. F. et al. Increase in forest water-use efficiency as atmospheric carbon dioxide concentrations rise. *Nature* **499**, 324–327 (2013).
31. Swann, A. L. S., Hoffman, F. M., Koven, C. D. & Randerson, J. T. Plant responses to increasing CO_2 reduce estimates of climate impacts on drought severity. *Proc. Natl Acad. Sci.* **113**, 10019–10024 (2016).
32. Zheng, B. et al. Record-high CO $_2$ emissions from boreal fires in 2021. *Science* **379**, 912–917 (2023).
33. Abatzoglou, J. T. & Williams, A. P. Impact of anthropogenic climate change on wildfire across western US forests. *Proc. Natl Acad. Sci.* **113**, 11770–11775 (2016).
34. Hudiburg, T. et al. Terrestrial carbon dynamics in an era of increasing wildfire. *Nat. Clim. Chang.* **13**, 1306–1316 (2023).
35. Fan, L. et al. Siberian carbon sink reduced by forest disturbances. *Nat. Geosci.* **16**, 56–62 (2023).
36. Anderegg, W. R. L., Kane, J. M. & Anderegg, L. D. L. Consequences of widespread tree mortality triggered by drought and temperature stress. *Nat. Clim. Change* **3**, 30–36 (2013).
37. Yan, Y. et al. Climate-induced tree-mortality pulses are obscured by broad-scale and long-term greening. *Nat. Ecol. Evol.* **8**, 912–923 (2024).
38. Ogle, K. et al. Quantifying ecological memory in plant and ecosystem processes. *Ecol. Lett.* **18**, 221–235 (2015).
39. Lian, X. et al. Diminishing carryover benefits of earlier spring vegetation growth. *Nat. Ecol. Evol.* **8**, 218–228 (2024).
40. Jump, A. S. et al. Structural overshoot of tree growth with climate variability and the global spectrum of drought-induced forest dieback. *Glob. Change Biol.* **23**, 3742–3757 (2017).
41. Willey, N. *Environmental Plant Physiology*. https://doi.org/10.1201/9781317206231 (Garland Science, New York, 2018).
42. Morellato, L. P. C. et al. Linking plant phenology to conservation biology. *Biol. Conserv.* **195**, 60–72 (2016).
43. Peters, M. K. et al. Climate–land-use interactions shape tropical mountain biodiversity and ecosystem functions. *Nature* **568**, 88–92 (2019).
44. Schumacher, D. L. et al. Amplification of mega-heatwaves through heat torrents fuelled by upwind drought. *Nat. Geosci.* **12**, 712–717 (2019).
45. Wright, A., Schnitzer, S. A. & Reich, P. B. Daily environmental conditions determine the competition–facilitation balance for plant water status. *J. Ecol.* **103**, 648–656 (2015).
46. Xu, X., Riley, W. J., Koven, C. D., Jia, G. & Zhang, X. Earlier leaf-out warms air in the north. *Nat. Clim. Chang.* **10**, 370–375 (2020).
47. Mohammadi, K., Jiang, Y. & Wang, G. Flash drought early warning based on the trajectory of solar-induced chlorophyll fluorescence. *Proc. Natl Acad. Sci.* **119**, e2202767119 (2022).
48. Wong, N. H., Tan, C. L., Kolokotsa, D. D. & Takebayashi, H. Greenery as a mitigation and adaptation strategy to urban heat. *Nat. Rev. Earth Environ.* **2**, 166–181 (2021).
49. Ng, E., Chen, L., Wang, Y. & Yuan, C. A study on the cooling effects of greening in a high-density city: an experience from Hong Kong. *Build. Environ.* **47**, 256–271 (2012).
50. Wong, N. H. & Yu, C. Study of green areas and urban heat island in a tropical city. *Habitat Int.* **29**, 547–558 (2005).
51. Ghanbari, M., Arabi, M., Georgescu, M. & Broadbent, A. M. The role of climate change and urban development on compound dry-hot extremes across US cities. *Nat. Commun.* **14**, 3509 (2023).
52. Zheng, Z., Zhao, L. & Oleson, K. W. Large model structural uncertainty in global projections of urban heat waves. *Nat. Commun.* **12**, 3736 (2021).
53. Zheng, B. et al. Record-high CO2 emissions from boreal fires in 2021. *Science* **379**, 912–917 (2023).
54. Miner, K. R. et al. Permafrost carbon emissions in a changing Arctic. *Nat. Rev. Earth Environ.* **3**, 55–67 (2022).
55. Gentine, P., Ferguson, C. R. & Holtslag, A. A. M. Diagnosing evaporative fraction over land from boundary-layer clouds. *J. Geophys. Res.: Atmospheres* **118**, 8185–8196 (2013).
56. Schuur, E. A. G. et al. Permafrost and climate change: carbon cycle feedbacks from the warming Arctic. *Annu. Rev. Environ. Resour.* **47**, 343–371 (2022).
57. Dai, A. Increasing drought under global warming in observations and models. *Nat. Clim. Change* **3**, 52–58 (2013).
58. Dai, A. Drought under global warming: a review. *WIREs Clim. Change* **2**, 45–65 (2011).
59. Giorgi, F., Coppola, E. & Raffaele, F. A consistent picture of the hydroclimatic response to global warming from multiple indices: Models and observations. *J. Geophys. Res.: Atmospheres* **119**, 11,695–11,708 (2014).
60. Kosaka, Y. & Xie, S.-P. Recent global-warming hiatus tied to equatorial Pacific surface cooling. *Nature* **501**, 403–407 (2013).
61. Liang, Y., Gillett, N. P. & Monahan, A. H. Climate model projections of 21st century global warming constrained using the observed warming trend. *Geophys. Res. Lett.* **47**, e2019GL086757 (2020).
62. Meehl, G. A., Teng, H. & Arblaster, J. M. Climate model simulations of the observed early-2000s hiatus of global warming. *Nat. Clim. Change* **4**, 898–902 (2014).
63. Yang, Y. et al. Evapotranspiration on a greening. *Earth. Nat. Rev. Earth Environ.* **4**, 626–641 (2023).
64. Berg, A., Sheffield, J. & Milly, P. C. D. Divergent surface and total soil moisture projections under global warming. *Geophys. Res. Lett.* **44**, 236–244 (2017).
65. Yuan, S., Quiring, S. M. & Leasor, Z. T. Historical changes in surface soil moisture over the contiguous united states: an assessment of CMIP6. *Geophys. Res. Lett.* **48**, e2020GL089991 (2021).
66. Lemordant, L., Gentine, P., Swann, A. S., Cook, B. I. & Scheff, J. Critical impact of vegetation physiology on the continental hydrologic cycle in response to increasing CO2. *Proc. Natl Acad. Sci.* **115**, 4093–4098 (2018).
67. Zhu, Z. et al. Global data sets of vegetation leaf area index (LAI)3 g and fraction of photosynthetically active radiation (FPAR)3g derived from global inventory modeling and mapping studies (GIMMS) normalized difference vegetation index (NDVI3g) for the period 1981 to 2011. *Remote Sens.* **5**, 927–948 (2013).
68. Xiao, Z. et al. Use of general regression neural networks for generating the GLASS leaf area index product from time-series MODIS surface reflectance. *IEEE Trans. Geosci. Remote Sens.* **52**, 209–223 (2014).

69. Jones, C. D. et al. C4MIP–the coupled climate–carbon cycle model intercomparison project: experimental protocol for CMIP6. *Geoscientific Model Dev.* **9**, 2853–2880 (2016).
70. Fowler, M. D., Kooperman, G. J., Randerson, J. T. & Pritchard, M. S. The effect of plant physiological responses to rising CO_2 on global streamflow. *Nat. Clim. Chang.* **9**, 873–879 (2019).
71. Dißmann, J., Brechmann, E. C., Czado, C. & Kurowicka, D. Selecting and estimating regular vine copulae and application to financial returns. *Computational Stat. Data Anal.* **59**, 52–69 (2013).
72. Fasola, S., Muggeo, V. M. R. & Küchenhoff, H. A heuristic, iterative algorithm for change-point detection in abrupt change models. *Comput Stat.* **33**, 997–1015 (2018).
73. Alkama, R. et al. Vegetation-based climate mitigation in a warmer and greener World. *Nat. Commun.* **13**, 606 (2022).
74. Bernacchi, C. J. & VanLoocke, A. Terrestrial ecosystems in a changing environment: a dominant role for water. *Annu. Rev. Plant Biol.* **66**, 599–622 (2015).
75. Bastos, A. et al. Direct and seasonal legacy effects of the 2018 heat wave and drought on European ecosystem productivity. *Sci. Adv.* **6**, eaba2724 (2020).
76. Buermann, W. et al. Widespread seasonal compensation effects of spring warming on northern plant productivity. *Nature* **562**, 110–114 (2018).
77. Buermann, W., Bikash, P. R., Jung, M., Burn, D. H. & Reichstein, M. Earlier springs decrease peak summer productivity in North American boreal forests. *Environ. Res. Lett.* **8**, 024027 (2013).
78. Luyssaert, S. et al. Land management and land-cover change have impacts of similar magnitude on surface temperature. *Nat. Clim. Change* **4**, 389–393 (2014).
79. Forzieri, G. et al. Increased control of vegetation on global terrestrial energy fluxes. *Nat. Clim. Chang.* **10**, 356–362 (2020).
80. Humphrey, V. et al. Soil moisture–atmosphere feedback dominates land carbon uptake variability. *Nature* **592**, 65–69 (2021).
81. Geladi, P. & Kowalski, B. R. Partial least-squares regression: a tutorial. *Analytica Chim. Acta* **185**, 1–17 (1986).
82. Zarakas, C. M., Swann, A. L. S., Laguë, M. M., Armour, K. C. & Randerson, J. T. Plant physiology increases the magnitude and spread of the transient climate response to CO_2 in CMIP6 earth system models. *J. Clim.* **33**, 8561–8578 (2020).

Acknowledgements

This study is supported by National Key Research and Development Program of China (2023YFF0805700). J.L. acknowledges the National Natural Science Foundation of China (42301106). E.B. and J.Z. acknowledge funding from the European Union's Horizon 2020 research and innovation program under grant agreement No 101003469 (XAIDA). J.Z. acknowledges the Helmholtz Initiative and Networking Fund (Young Investigator Group COMPOUNDX, Grant Agreement VH-NG-1537). E.B. received funding from the Deutsche Forschungsgemeinschaft (DFG, German Research Foundation) via the Emmy Noether Program (grant ID 524780515). T.F.K. acknowledges support from the RUBISCO SFA, which is sponsored by the Regional and Global Model Analysis (RGMA) Program in the Climate and Environmental Sciences Division (CESD) of the Office of Biological and Environmental Research (BER) in the U.S. Department of Energy (DOE) Office of Science, and additional support from a DOE Early Career Research Program award #DE-SC0021023, and NASA awards 80NSSC20K1801 & 80NSSC25K7327. X.L. and T.F.K. acknowledge support from the LEMONTREE (Land Ecosystem Models based On New Theory, obseRvations and ExperimEnts) project, funded through the generosity of Eric and Wendy Schmidt by recommendation of the Schmidt Futures program. This work is supported by the High-performance Computing Platform of Peking University.

Author contributions

Y.Z. conceived the idea. Y.Z. and J.L. designed the study, with contributions from S.P. J.L. performed the analysis, J.L. and Y.Z. wrote the manuscript. J.L., Y.Z., E.B., J.Z., T.F.K., X.L., S.Z., H.Z., M.H., S.P. discussed and commented on the results and the manuscript.

Competing interests

The authors declare no competing interests.

Additional information

Supplementary information The online version contains supplementary material available at https://doi.org/10.1038/s41467-024-55175-0.

Correspondence and requests for materials should be addressed to Yao Zhang.

Peer review information *Nature Communications* thanks the anonymous reviewers for their contribution to the peer review of this work. A peer review file is available.

Reprints and permissions information is available at http://www.nature.com/reprints